

www.acsaem.org Article

High-Performance Perovskite Solar Cells by One-Step Self-Assembled Perovskite-Polymer Thin Films

Luyao Zheng, Kai Wang, Tao Zhu, Yongrui Yang, Rui Chen, Kai Gu, Chunming Liu, and Xiong Gong*



Cite This: https://dx.doi.org/10.1021/acsaem.0c00823



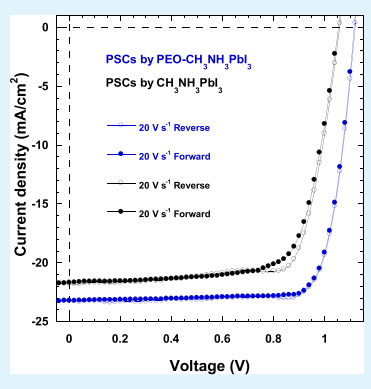
ACCESS

III Metrics & More

Article Recommendations

SI Supporting Information

ABSTRACT: Perovskite materials have drawn the greatest attention as alternatives for approaching cost-effective perovskite solar cells (PSCs) in the past decade. However, the desire for PSCs with photocurrent hysteresis-free characteristics has been unfulfilled due to the intrinsic foibles of perovskite materials. In this study, PSCs with boosted power conversion efficiency (PCEs), dramatically suppressed photocurrent hysteresis, and significantly boosted stability through one-step self-assembled methylammonium lead iodide (CH₃NH₃PbI₃) cocrystallized with poly(ethylene oxide) (PEO) are reported. It is found that one-step self-assembled CH₃NH₃PbI₃ cocrystallized with PEO could generate high-quality thin film with significantly enlarged crystal grains through weak hydrogen interactions between CH₃NH₃PbI₃ and PEO. Further studies demonstrate that one-step self-assembled PEO—CH₃NH₃PbI₃ thin films possess improved charge carrier transport, reduced charge carrier recombination, and promoted charge carrier extraction time as compared with those of one-step self-assembled PEO—Theorem PEO—T



CH₃NH₃PbI₃ thin films exhibit a PCE of 20.78%, which is an over 20% enhancement compared to that (17.42%) from PSCs by one-step self-assembled CH₃NH₃PbI₃ thin films. Moreover, PSCs by one-step self-assembled PEO-CH₃NH₃PbI₃ thin films exhibit dramatically suppressed photocurrent hysteresis and significantly boosted stability. All these results demonstrate that the method of one-step self-assembled perovskites cocrystallized with polymers is a facile approach toward high-performance PSCs.

KEYWORDS: hybrid perovskites, one-step self-assembly, cocrystallization, poly(ethylene oxide), photocurrent hysteresis, power conversion efficiency and stability

1. INTRODUCTION

In the past decade, organic-inorganic hybrid perovskites with a typical chemical formula of ABX3, where the A-site cation is methylammonium (CH₃NH₃⁺), formamidinium (NH₂CH= NH₂⁺), or Cs⁺; the B-site cation is Pb²⁺ or Sn²⁺; and the X-site anion is Cl-, Br-, or I-, or their combination, have been extensively studied for approaching efficient low-cost solutionprocessed perovskite solar cells (PSCs).^{1,2} Power conversion efficiencies (PCEs) exceeding 25% have been observed from PSCs by high-quality hybrid perovskite thin films.³ However, it was found that PSCs were with abnormal photocurrent hysteresis behaviors, which restricted their practical applications. 1-9 Studies revealed that the photocurrent hysteresis partially originated from the surface defects and counterions migration within the perovskite thin films. 5-9 Many approaches have been attempted to suppress photocurrent hysteresis. 10-14 By utilization of an ultrathin layer of 4-lithium styrenesulfonic acid/styrene ionomer copolymer to passivate solution-processed CH3NH3PbI3 thin film, we found that photocurrent hysteresis was dramatically suppressed in PSCs. 10 It was also reported that ionic liquids and polymers as the additives could freeze counterions migration and manipulate perovskite crystallization through weak interactions between ionic liquids (or polymers) with counterions in the A-, B-, and X-sites in perovskites. ^{11–14} For instance, Seo et al. reported utilization of methylammonium liquid crystals to control perovskite crystal growth to realize compact perovskite films with a large crystalline domain for approaching PSCs with suppressed photocurrent hysteresis. ¹¹ Bai et al. observed dramatically reduced photocurrent hysteresis from PSCs, where perovskite crystals were linked with 1-butyl-3-methylimidazolium tetrafluoroborate liquid crystals. ¹² Recently, our group demonstrated hysteresis-free efficient PSCs, where perovskites were cocrystallized with poly(ethylene oxide) (PEO). ¹³

PSCs by CH₃NH₃PbI₃ thin films with dramatically suppressed photocurrent hysteresis were reported, where CH₃NH₃PbI₃ thin films were prepared by the two-step method. 11–14 Recently, efficient PSCs were reported, where high-quality CH₃NH₃PbI₃ thin films were prepared by a one-step self-assembling method. 15,16 Different to the two-step

Received: April 13, 2020 **Accepted:** May 15, 2020 **Published:** May 15, 2020



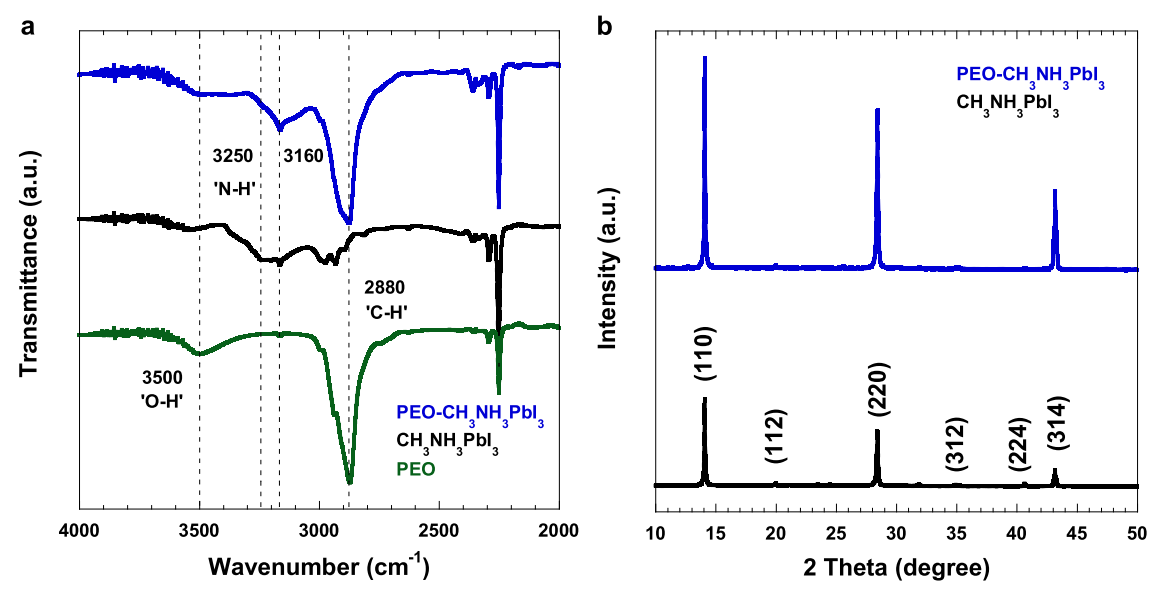


Figure 1. (a) The FTIR spectra of CH₃NH₃PbI₃ and PEO-CH₃NH₃PbI₃ precursor solutions and PEO solution, and (b) the XRD patterns of CH₃NH₃PbI₃ and PEO-CH₃NH₃PbI₃ thin films.

method, in the one-step self-assembling process, low boiling point solvents, for example, acetonitrile (ACN), rather than high boiling point solvents, for example, dimethylformamide (DMF) and dimethyl sulfoxide (DMSO), were used for making CH₃NH₃PbI₃ solutions and then casting thin films. ^{15,16} The precursor solution was obtained by the exfoliation of CH3NH3PbI3 single crystals into liquid layered perovskite intermediates rather than CH3NH3I:PbI2 mixed solutions. 11,12,14 In the one-step self-assembly process, no ACN-PbI₂ intermediate was formed and no antisolvent was required to produce high-quality CH₃NH₃PbI₃ thin films since CH₃NH₃PbI₃ thin films were directly formed by casting liquid layered perovskite intermediates during the fast volatilization of ACN. Thus, PSCs by one-step self-assembling processed CH₃NH₃PbI₃ thin films exhibited enhanced PCEs. 15,16 However, to the best of our knowledge, the photocurrent hysteresis behaviors of PSCs by one-step self-assembled CH₃NH₃PbI₃ thin film have not been reported so far.

In this study, we report high-performance PSCs by one-step self-assembled PEO-CH₃NH₃PbI₃ thin films. It is found that one-step self-assembled PEO-CH₃NH₃PbI₃ thin films possess a high quality with significantly enlarged crystal grains, as compared to the one-step self-assembled CH3NH3PbI3 thin film. Systematical investigations reveal that that one-step selfassembled PEO-CH3NH3PbI3 thin films exhibit improved charge transport, reduced charge carrier recombination, and promoted charge extraction time. As a result, PSCs by the onestep self-assembled PEO-CH3NH3PbI3 thin films exhibit a boosted PCE of 20.78%, which is an over 20% enhancement compared to that (17.42%) from PSCs by one-step selfassembled CH3NH3PbI3 thin films. Moreover, PSCs by onestep self-assembled PEO-CH3NH3PbI3 thin films exhibit dramatically suppressed photocurrent hysteresis and significantly boosted stability.

2. MATERIALS AND METHODS

2.1. Materials. Lead iodide (PbI₂, 99.9985%, metals basis) was purchased from Alfa Aesar. PEO with molecular weight (Mw) of 1000 Da was purchased from Scientific Polymer, Inc. Methylammonium iodide (CH₃NH₃I, 99.9%) was purchased from GreatCell Solar. [6,6]-

Phenyl- C_{61} -butyric acid methyl ester (PC $_{61}$ BM, 99.5%) was purchased from Solenne BV. Gamma-butyrolactone (GBL, 99%), methylamine (33 wt % in absolute ethanol), anhydrous acetonitrile (ACN, 99.8%), poly[bis(4-phenyl)(2,4,6-trimethylphenyl)amine] (PTAA), toluene (99.8%), bathocuproine (BCP, 99.99%), and chlorobenzene (CB, 99.8%) were purchased from Sigma-Aldrich. All chemicals were used as received, and no further purification was conducted.

2.2. $\text{CH}_3\text{NH}_3\text{PbI}_3$ Single Crystals. The growth of $\text{CH}_3\text{NH}_3\text{PbI}_3$ single crystals follows an inverse temperature crystallization method. The Briefly, 1 mmol of PbI_2 and 1 mmol of $\text{CH}_3\text{NH}_3\text{I}$ were dissolved into 1 mL of GBL, and then the solution was kept continually stirring until it reached a yellowish—clear solution. Afterward, the solution was heated to 110 °C to allow the single crystals to grow naturally. Black single crystals were obtained, rinsed with isopropanol solvent several times, and then dried in an oven for 10 min.

2.3. Perovskite Precursor Solution. CH₃NH₃PbI₃ ACN solution was prepared with the method reported in the literature.¹⁵ CH₃NH₃PbI₃ single crystals were placed in a small vial without a cap, and then the small vial was placed into a large bottle containing methylamine mixed with ethanol solutions. In such case, methylamine vapor diffused into the small vial and exfoliated CH₃NH₃PbI₃ single crystals into a viscous yellow solution. Afterward, ACN was added into the above yellow solution to make 1 mol L⁻¹ CH₃NH₃PbI₃ ACN solution. For PEO-CH₃NH₃PbI₃ solution, a certain amount (to adjust the ratios of PEO to CH₃NH₃PbI₃) of PEO ACN solution was mixed with CH₃NH₃PbI₃ ACN solution.

2.4. Preparation and Characterizations of Perovskite Thin Films. Both CH₃NH₃PbI₃ thin film and PEO-CH₃NH₃PbI₃ thin film on either bare glass substrates or indium-doped tin oxide (ITO)coated glass substrates were prepared by the spin-casting method from their corresponding precursor solutions at 6000 rpm spin-speed for 30 s (s) and then were thermally annealed at 100 °C for 10 min. Attenuated total reflectance Fourier-transform infrared (ATR-FTIR) spectra were measured on a Thermo Scientific Nicolet 380 FTIR spectrometer. X-ray diffraction (XRD) patterns of perovskite thin films were obtained from a Bruker AXS Dimension D8 X-ray system. An HP 8453 spectrophotometer was utilized for ultraviolet-visible (UV-vis) absorption spectra of perovskite thin films. A Picoharp 300 instrument after preamplification by PAM 102 was used for measuring the photoluminescence (PL) spectra of perovskite thin films. The objective-type total internal reflection fluorescence microscopy (TIRFM) images of individual CH₃NH₃PbI₃ and PEO-CH₃NH₃PbI₃ crystal grains were imaged at 532 nm laser excitation. Filtered by a 542 nm long-pass filter, the PL of particles was collected by a CMOS

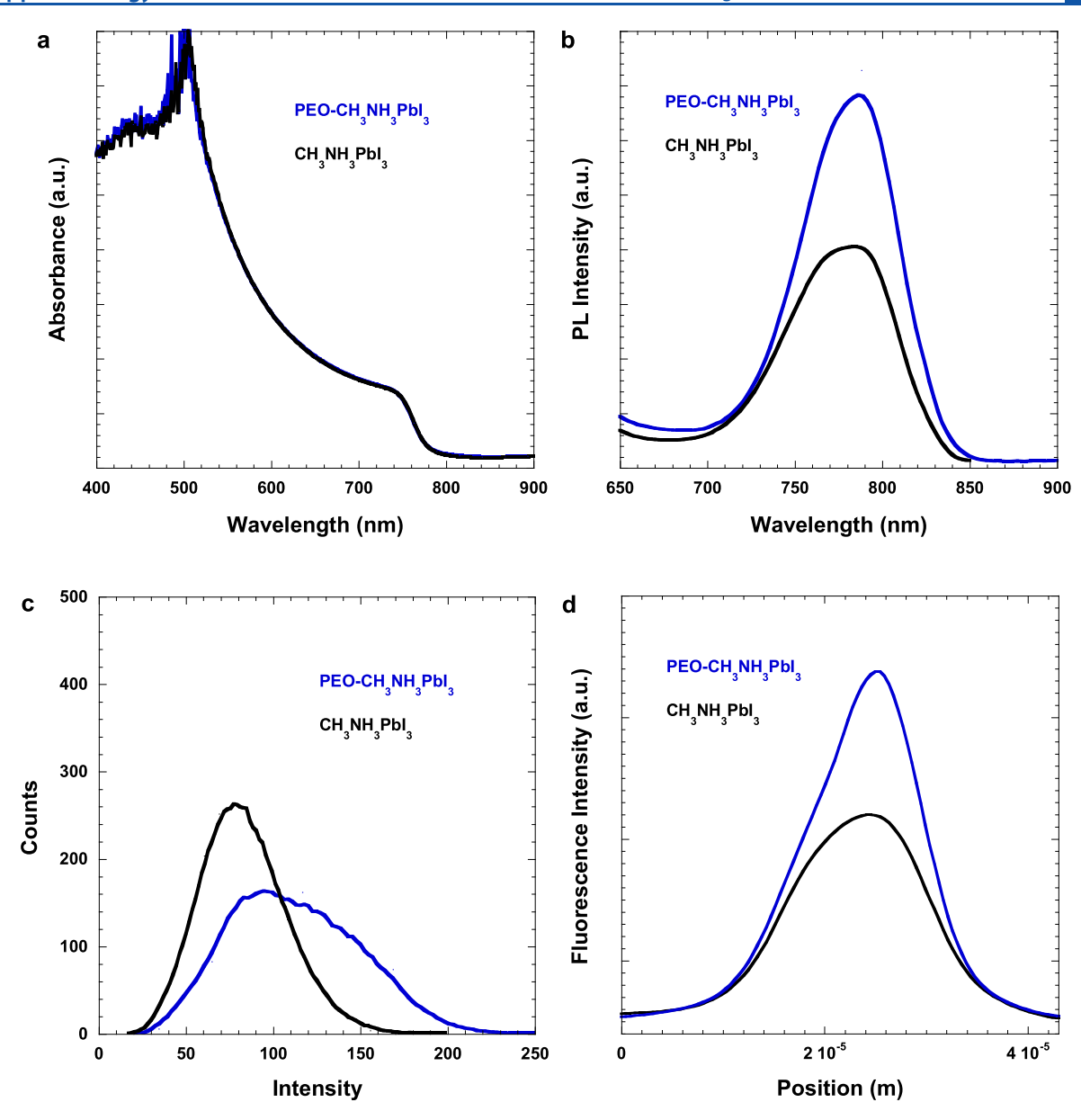


Figure 2. (a) The absorption and (b) PL spectra of CH₃NH₃PbI₃ and PEO-CH₃NH₃PbI₃ thin films; (c) the PL intensity histogram and (d) the line profile of TIRFM of CH₃NH₃PbI₃ and PEO-CH₃NH₃PbI₃ crystal grains.

camera. Under each experimental condition, 1000 consecutive images of perovskite particles were taken with 50 ms exposure time. A field-emission scanning electron microscope (JEOL-7401) was applied to obtain the top-view scanning electron microscopy (SEM) images. A DektakXT surface profile system was used to measure the thin film thickness of $CH_3NH_3PbI_3$ and $PEO-CH_3NH_3PbI_3$ thin films.

2.5. Fabrication of PSCs. An approximately 8 nm PTAA thin layer was deposited on precleaned and treated ITO-coated glass substrates from 2 mg mL⁻¹ toluene solution and was thermally annealed at 100 °C for 10 min. Both CH₃NH₃PbI₃ and PEO–CH₃NH₃PbI₃ thin films were deposited on the top of the PTAA layer with the method described above. After that, an ~40 nm PC₆₁BM layer was casted on the top of the perovskite layer from 20 mg mL⁻¹ chlorobenzene solution. Finally, an ~8 nm BCP thin layer and 100 nm aluminum (Al) layer were thermally deposited on the top of the PC₆₁BM layer in a vacuum at ~9 × 10^{-6} mbar. The active area was measured to be 0.045 cm².

2.6. Characterization of PSCs. The current density—voltage (J-V) characteristics and the external quantum efficiency (EQE) spectra of PSCs were measured with the method reported in our previous publications. ^{10,13} The detailed impedance spectroscopy (IS), the

capacitance versus frequency (C-F), and capacitance versus voltage (C-V) measurements, as well as the transient photocurrent (TPC) measurements, can be found in our previous report or elsewhere. ^{13,18}

3. RESULTS AND DISCUSSION

ATR-FTIR spectroscopy was conducted to confirm that PEO interacted with CH₃NH₃⁺ counterions to form a hydrogen bond of 'O···H-NH₂CH₃⁺' at the crystal-A-site in CH₃NH₃PbI₃ solution. Figure 1a presents the FTIR spectra of CH₃NH₃PbI₃ and PEO-CH₃NH₃PbI₃ precursor solutions and PEO solution. As compared with CH₃NH₃PbI₃ solution, two new peaks are observed from both PEO and PEO-CH₃NH₃PbI₃ solutions. A weak "O-H" stretching vibration at ~3500 cm⁻¹, originating from the inter- and intramolecular hydrogen bonds, ^{14,19} and a sharp "C-H" stretching vibration at ~2880 cm⁻¹, corresponding to the backbone of PEO, ¹⁹ are observed from PEO and PEO-CH₃NH₃PbI₃ solutions, which demonstrate that PEO is present in PEO-CH₃NH₃PbI₃ solution. However, the "O-H" stretching vibration in PEO-

CH₃NH₃PbI₃ solution is weaker and broader than that in PEO solution. These results indicate that PEO has interacted with CH₃NH₃PbI₃ in PEO-CH₃NH₃PbI₃ solution. Moreover, it is found that two "N-H" stretching bands at ~3250 cm-1 and ~3160 cm⁻¹ are observed from CH₃NH₃PbI₃ solution.² Whereas, only a single "N−H" stretching band at ~3160 cm⁻¹ is observed from PEO-CH3NH3PbI3 solution. The diminishing of the "N-H" stretching band at ~3250 cm⁻¹ could be attributed to the formation of 'O···H-NH2CH3+' interaction. 13,21,22 All these results demonstrate that the 'O···H-NH2CH3+ interaction takes place between PEO and CH₃NH₃PbI₃ in PEO-CH₃NH₃PbI₃ solution. Such hydrogen interaction in PEO-CH3NH3PbI3 solution could affect the crystallization of PEO-CH₃NH₃PbI₃ thin films, ^{13,15} suppress the counterions migration, and minimize the defects within PEO-CH₃NH₃PbI₃ thin films. 13

Figure 1b displays the XRD patterns of CH3NH3PbI3 and PEO-CH₃NH₃PbI₃ thin films. Both CH₃NH₃PbI₃ and PEO-CH₃NH₃PbI₃ thin films have a typical tetragonal crystal structure with the (110), (112), (220), (312), (224), and (314) planes. 13,17 However, negligible diffraction peaks ascribed to PEO are observed from PEO-CH3NH3PbI3 thin film, which indicates that the good dispersion of PEO in the perovskite crystal dominates rather than presents as the individual PEO aggregates. 13 Furthermore, the full-width at half-maximums (fwhms) of the (110), (220), and (314) planes for CH₃NH₃PbI₃ thin film are 0.128°, 0.165°, and 0.241°, respectively. Whereas, the fwhms of the (110), (220), and (314) planes for PEO-CH₃NH₃PbI₃ thin film are 0.116°, 0.164°, and 0.239°, respectively. The reduced fwhm values indicate larger and finer perovskite crystal domains formed in PEO-CH₃NH₃PbI₃ thin film, suggesting that PEO affects the crystallization of PEO-CH3NH3PbI3 thin films due to the formation of 'O···H-NH2CH3+' hydrogen bond between PEO and CH₂NH₂PbI₂.

Figure 2a presents the absorption spectra of both CH₃NH₃PbI₃ and PEO-CH₃NH₃PbI₃ thin films. Both thin films exhibit identical absorption spectra, indicating that PEO has no effect on the band structure of CH₃NH₃PbI₃ thin film.

Figure 2b displays the PL spectra of both CH₃NH₃PbI₃ and PEO-CH₃NH₃PbI₃ thin films. The PL shapes of CH₃NH₃PbI₃ and PEO-CH₃NH₃PbI₃ thin films are identical, but the PL intensity of PEO-CH₃NH₃PbI₃ thin film is much higher than that of CH₃NH₃PbI₃ thin film. These results demonstrate that the nonradiative recombination process in PEO-CH₃NH₃PbI₃ thin film is suppressed. Such suppressed nonradiative recombination implies that the trap states and defects in PEO-CH₃NH₃PbI₃ thin film are minimized. ^{15,23}

The TIRFM is further carried out to investigate PL profiles of individual CH₃NH₃PbI₃ and PEO-CH₃NH₃PbI₃ crystal grains. Figure 2c presents the PL intensity histogram of individual CH₃NH₃PbI₃ and PEO-CH₃NH₃PbI₃ crystal grains in the 1000 frames, which are observed from the TIRFM images as shown in Figure S1. It is found that CH₃NH₃PbI₃ crystal grains exhibit an average PL intensity of 75, whereas PEO-CH₃NH₃PbI₃ crystal grains exhibit an average PL intensity of 120. The enhancement in PL intensity indicates that the nonradiative recombination in PEO-CH₃NH₃PbI₃ crystal grains is suppressed. Figure 2d presents the average line profiles at the same position of TIRFM for both CH₃NH₃PbI₃ and PEO-CH₃NH₃PbI₃ crystal grains. It is clear that PEO-CH₃NH₃PbI₃ crystal grains exhibit more intense PL as compared with that of CH₃NH₃PbI₃ crystal grains. These

observations are consistent with the PL intensities observed from both CH₃NH₃PbI₃ and PEO-CH₃NH₃PbI₃ thin films. These results further confirm that PEO could minimize the trap states and the defects, resulting in suppressed nonradiative recombination in PEO-CH₃NH₃PbI₃ thin film.

Figure 3 presents the top-view SEM images of CH₃NH₃PbI₃ and PEO-CH₃NH₃PbI₃ thin films. The CH₃NH₃PbI₃ thin

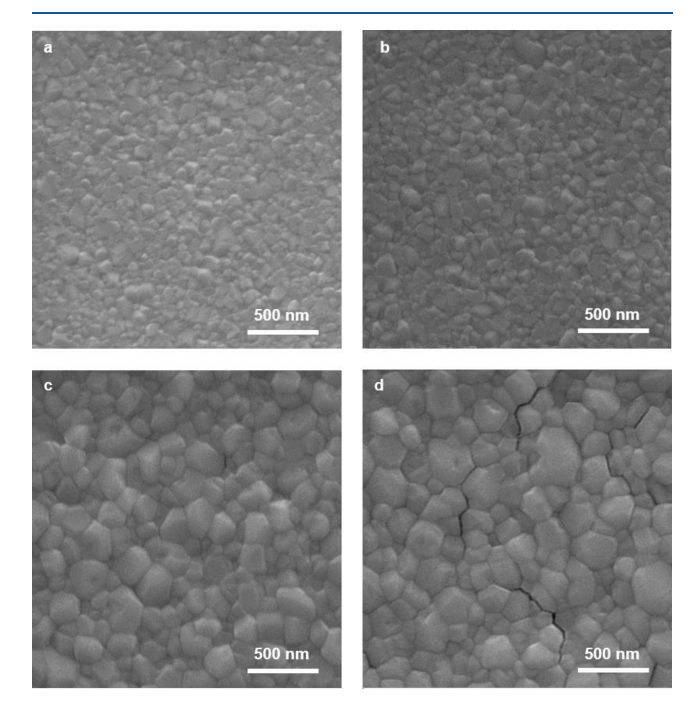


Figure 3. Top-view SEM images of (a) $CH_3NH_3PbI_3$ thin film, (b) $PEO-CH_3NH_3PbI_3$ thin film with 0.05% PEO, (c) $PEO-CH_3NH_3PbI_3$ thin film with 0.1% PEO, and (d) $PEO-CH_3NH_3PbI_3$ thin film with 0.5% PEO.

film possesses close-packed crystals with an average grain size of $\sim\!100$ nm. The crystal size of PEO–CH₃NH₃PbI₃ thin film with 0.05% concentration of PEO is slightly enlarged to $\sim\!120$ nm. Moreover, the crystal size of PEO–CH₃NH₃PbI₃ thin film with 0.1% concentration of PEO is dramatically enlarged to $\sim\!200$ nm. However, many cracks are observed from PEO–CH₃NH₃PbI₃ thin film with 0.5% concentration of PEO even if its crystal size is enlarged to $\sim\!250$ nm. These results indicate that PEO plays an important role in the crystallization of PEO–CH₃NH₃PbI₃ thin film.

The photovoltaic properties of one-step self-assembled PEO-CH₃NH₃PbI₃ thin film is investigated and compared with one-step self-assembling processed CH₃NH₃PbI₃ thin film through characterization of PSCs with a device structure of ITO/PTAA/PEO-CH₃NH₃PbI₃/PC₆₁BM/BCP/Al, where ITO is used as the anode, PTAA is used as the hole transport layer, PC61BM is used as the electron transport layer, BCP serves as the hole-blocking layer, and Al serves as the cathode. The J-V characteristics with a scan rate of 20 V/s under the reverse scan direction are presented in Figure 4a. The PSCs by $CH_3NH_3PbI_3$ thin film exhibit a short-circuit current (J_{SC}) of 22.21 mA cm $^{-2}$, an open-circuit voltage ($V_{\rm OC}$) of 1.04 V, a fill factor (FF) of 0.75, and a corresponding PCE of 17.32%. These device performance parameters are in good agreement with reported values from PSCs with similar device structures. 15,16 The PSCs by PEO-CH₃NH₃PbI₃ thin film, where the concentration of PEO is at 0.05%, exhibit a J_{SC} of

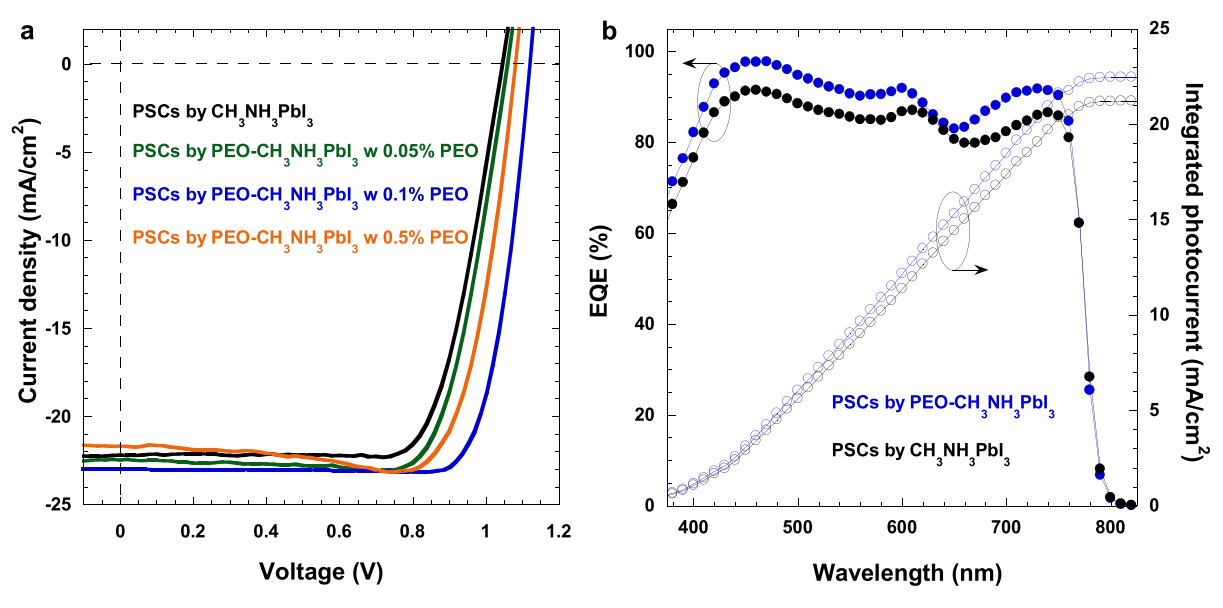


Figure 4. (a) The *J-V* characteristics of PSCs by either CH₃NH₃PbI₃ thin film or PEO-CH₃NH₃PbI₃ thin films with different PEO concentrations, and (b) the EQE spectra and integrated photocurrent of PSCs by either CH₃NH₃PbI₃ or PEO-CH₃NH₃PbI₃ thin films.

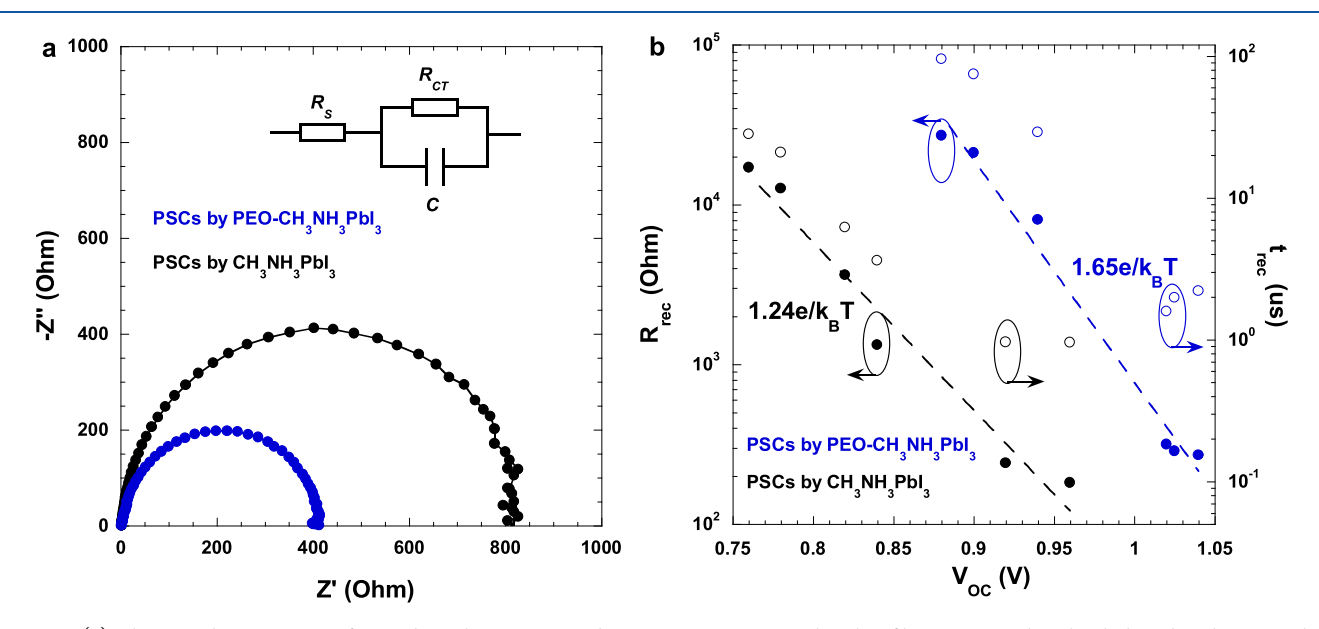


Figure 5. (a) The impedance spectra of PSCs by either $CH_3NH_3PbI_3$ or $PEO-CH_3NH_3PbI_3$ thin films, measured in the dark and under an applied bias close to V_{OC} , and (b) the recombination resistance and recombination lifetime of PSCs by either $CH_3NH_3PbI_3$ or $PEO-CH_3NH_3PbI_3$ thin films.

22.48 mA cm⁻², a $V_{\rm OC}$ of 1.06 V, an FF of 0.77, and a corresponding PCE of 18.27%. The PSCs by PEO—CH₃NH₃PbI₃ thin film, where the concentration of PEO is at 0.1%, exhibit a $J_{\rm SC}$ of 23.01 mA cm⁻², a $V_{\rm OC}$ of 1.12 V, an FF of 0.81, and a corresponding PCE of 20.78%, which is ~20% enhancement compared to that by CH₃NH₃PbI₃ thin film. However, the PSCs by PEO—CH₃NH₃PbI₃ thin film, where the concentration of PEO is at 0.5%, exhibit a $J_{\rm SC}$ of 21.70 mA cm⁻², a $V_{\rm OC}$ of 1.08 V, an FF of 0.81, and a corresponding PCE of 19.04%. Such inferior device performance is ascribed to poor film morphology with cracks induced by excess PEO (Figure 3d).

The EQE spectra of PSCs with integrated J_{SC} are shown in Figure 4b. As compared with PSCs by $CH_3NH_3PbI_3$ thin film, PSCs by PEO- $CH_3NH_3PbI_3$ thin film exhibit apparently increased EQE values in the wavelength from 375 to 750 nm.

Moreover, the integrated J_{SC} values of PSCs by CH₃NH₃PbI₃ thin film and PSCs by PEO-CH₃NH₃PbI₃ thin film are 21.21 and 22.46 mA cm⁻², respectively. These integrated J_{SC} values are consistent with those from the J-V characteristics (Figure 4a). Such enhanced EQE and J_{SC} values are attributed to the enlarged crystal sizes and suppressed nonradiative recombination process in PEO-CH₃NH₃PbI₃ thin film.

In order to investigate the enhancement in $J_{\rm SC}$, the IS measurement is carried out to study the charge transport and charge carrier recombination within PSCs. The Nyquist plots of IS spectra of PSCs measured in the dark and under the applied bias close to $V_{\rm OC}$ are presented in Figure 5a. In such conditions, the charge carrier recombination resistance ($R_{\rm rec}$) is minimized and the charge transport resistance ($R_{\rm CT}$) dominates in PSCs.²⁴ As a result, the $R_{\rm rec}$ is far smaller than the $R_{\rm CT}$. Thus, the equivalent circuit is simplified as the circuit

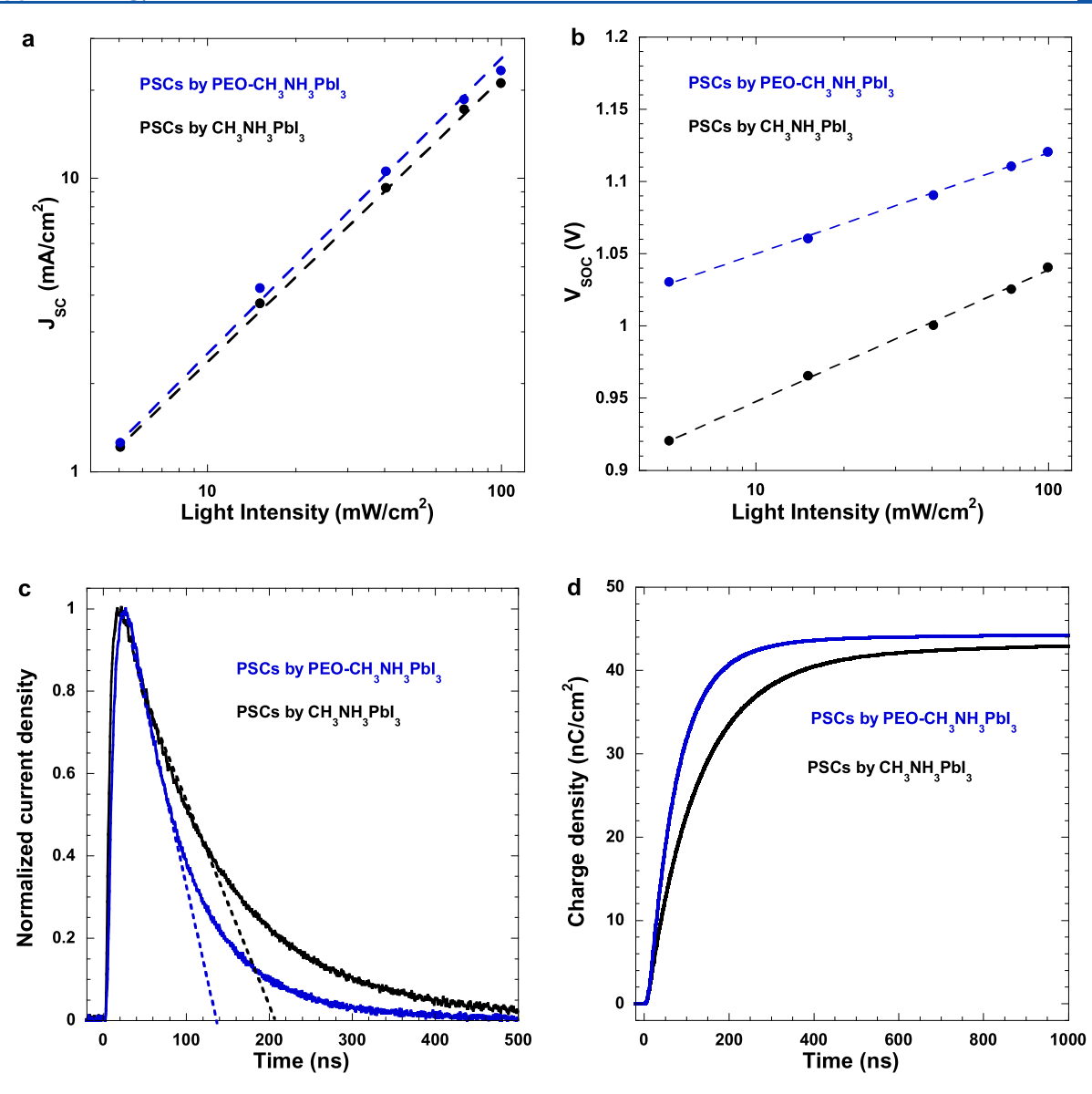


Figure 6. Light intensity dependent on (a) $V_{\rm OC}$ and (b) $J_{\rm SC}$ for PSCs by either CH₃NH₃PbI₃ or PEO-CH₃NH₃PbI₃ thin films, (c) the TPC characteristics of PSCs by either CH₃NH₃PbI₃ or PEO-CH₃NH₃PbI₃ thin films, and (d) integrated charge density of PSCs by either CH₃NH₃PbI₃ or PEO-CH₃NH₃PbI₃ thin films.

model as presented in the inset of Figure 5a, where $R_{\rm S}$ presents the sheet resistance of the electrodes. ^{24,25} Since the same device structure is applied, the $R_{\rm S}$ is assumed to be the same under this study. ²⁴ Thus, the difference in the $R_{\rm CT}$ is solely from the photoactive layer, i.e., ${\rm CH_3NH_3PbI_3}$ and PEO– ${\rm CH_3NH_3PbI_3}$ thin films. As shown in Figure 5a, both PSCs by ${\rm CH_3NH_3PbI_3}$ and PEO– ${\rm CH_3NH_3PbI_3}$ thin films exhibit one semicircle. The $R_{\rm CT}$ is obtained from the radius of the semicircle. The $R_{\rm CT}$ for PSCs by ${\rm CH_3NH_3PbI_3}$ thin film is 805 Ω , whereas the $R_{\rm CT}$ for PSCs by PEO– ${\rm CH_3NH_3PbI_3}$ thin film is 413 Ω . The decreased $R_{\rm CT}$ is attributed to the optimal film morphology with larger crystals of PEO– ${\rm CH_3NH_3PbI_3}$ thin film. Such dramatically reduced $R_{\rm CT}$ indicates that charge transport properties of PEO– ${\rm CH_3NH_3PbI_3}$ thin film are boosted. Therefore, enlarged $J_{\rm SC}$ is observed from PSCs by PEO– ${\rm CH_3NH_3PbI_3}$ thin film.

Figure 5b presents the correlation between the $R_{\rm rec}$ and $V_{\rm OC}$, where the $R_{\rm rec}$ is calculated based on the Nyquist plots at the low frequency region (Figure S2).²⁴ Under light illumination

and at the applied bias close to $V_{\rm OC}$, the $R_{\rm CT}$ is minimized and the $R_{\rm rec}$ dominates in PSCs. A larger $R_{\rm rec}$ from PSCs by PEO–CH₃NH₃PbI₃ thin film as compared with that by CH₃NH₃PbI₃ thin film indicate that charge carrier recombination in PSCs by PEO–CH₃NH₃PbI₃ thin film is dramatically suppressed. Thus, PSCs by PEO–CH₃NH₃PbI₃ thin film have enhanced $J_{\rm SC}$.

The $R_{\rm rec}$ correlated with $V_{\rm OC}$ is described as $R_{\rm rec}$ = R_0 exp $(-q\beta/2k_{\rm B}TV_{\rm OC}(I))$ (where R_0 is a constant, q is the electron charge, β is the recombination order parameter, $k_{\rm B}$ is the Boltzmann constant, T is the absolute temperature, and I is the light intensity, respectively). As shown in Figure 5b, PSCs by CH₃NH₃PbI₃ thin film exhibit a β of 1.24, which indicates the trap-assistant first-order charge carrier recombination is dominated in PSCs. A β of 1.65 is observed from PSCs by PEO-CH₃NH₃PbI₃ thin film, which illustrates that the second-order charge carrier recombination mechanism is dominated in PSCs. Thus, the trap-assistant charge carrier recombination is suppressed in PSCs by PEO-CH₃NH₃PbI₃

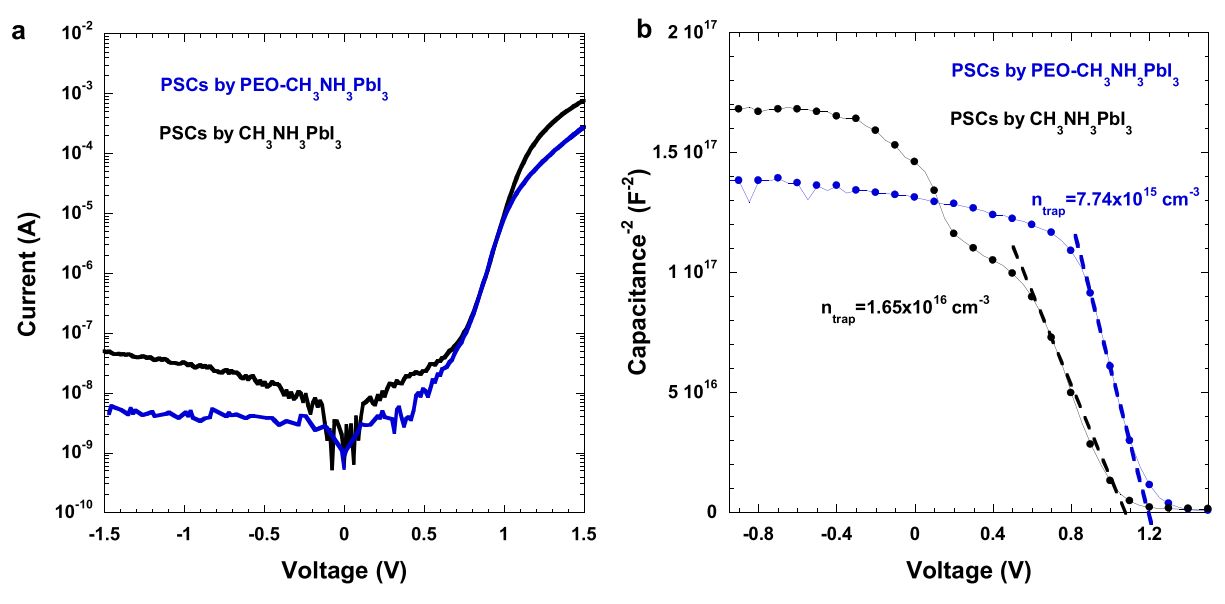


Figure 7. (a) The J-V characteristics of PSCs by either CH₃NH₃PbI₃ or PEO-CH₃NH₃PbI₃ thin films, measured in dark, and (b) the $C^{2-}V$ characteristics of PSCs by either CH₃NH₃PbI₃ or PEO-CH₃NH₃PbI₃ thin films.

thin film. As a result, PSCs by PEO- $CH_3NH_3PbI_3$ thin film haves boosted J_{SC} and FF.

In addition, the charge carrier recombination lifetime $(t_{\rm rec})$ correlated with different $V_{\rm OC}$ is estimated based on $t_{\rm rec} = R_{\rm rec}C_{\mu}$ (where C_{μ} is chemical capacitance). The $t_{\rm rec}$ is the average lifetime for free charge carrier prior to being recombined in PSCs. The charge carrier recombination lifetimes of PSCs by either CH₃NH₃PbI₃ thin film or PEO-CH₃NH₃PbI₃ thin film are shown in Figure 5b. Under the same condition, it is found that a $t_{\rm rec}$ of 2.2 μ s is observed from PSCs by PEO-CH₃NH₃PbI₃ thin film, whereas a $t_{\rm rec}$ of 0.9 μ s is observed from PSCs by CH₃NH₃PbI₃ thin film. Such prolonged $t_{\rm rec}$ from PSCs by PEO-CH₃NH₃PbI₃ thin film is ascribed to suppressed defects and traps states in PEO-CH₃NH₃PbI₃ thin film exhibit enhanced $t_{\rm SC}$.

The light intensity dependence of $J_{\rm SC}$ and $V_{\rm OC}$ are also studied, and the results are shown in Figure 6a, b. As indicated in Figure 6a, both PSCs exhibit power law dependency of $J_{\rm SC}$ on the light intensity. Based on $J_{\rm SC} \propto I^{\alpha}$ (where I is the light intensity and α is the coefficient), 30 α of 0.96 is observed from PSCs by CH₃NH₃PbI₃ thin film and α of 0.98 is observed from PSCs by PEO-CH₃NH₃PbI₃ thin film, respectively. As α closer to 1, a weaker nongeminate recombination takes place in PSCs by PEO-CH₃NH₃PbI₃ thin film. 30 Thus, PSCs by PEO-CH₃NH₃PbI₃ thin film exhibit enhanced $J_{\rm SC}$.

Moreover, as shown in Figure 6b, both PSCs exhibit a logarithmic relation of $V_{\rm OC}$ on I, which is described as $V_{\rm OC} \propto S \ln(I)$ (where S is the slope). A slope S of 1.52 $k_{\rm B}T/q$ (where $k_{\rm B}$ is the Boltzmann constant, q is the elementary charge, and T is the absolute temperature) is observed from PSCs by ${\rm CH_3NH_3PbI_3}$ thin film, indicating that both bimolecular charge carrier recombination and trap-assistant charge carrier recombination have taken place in PSCs; whereas, a smaller S of 1.17 $k_{\rm B}T/q$ is found from PSCs by PEO— $CH_3NH_3PbI_3$ thin film, demonstrating that suppressed trap-assistant recombination has taken place in PSCs. The reduced charge carrier recombination is consistent with the enhanced $J_{\rm SC}$ observed from PSCs by PEO— $CH_3NH_3PbI_3$ thin film.

The charge carrier extraction time in PSCs is investigated by TPC measurement. Figure 6c displays the normalized TPC curves of PSCs under an applied bias of -2 V. Under such high bias voltage, all charge carriers are swept out prior to recombination. Charge carrier transit time is estimated through extrapolating the linear region to aero photocurrent. The charge carrier extraction times from PSCs by either CH₃NH₃PbI₃ thin film or PEO–CH₃NH₃PbI₃ thin film are \sim 170 and \sim 112 ns, respectively. The shorter charge carrier extraction time demonstrates a more efficient charge extraction process in PSCs. Therefore, PSCs by PEO–CH₃NH₃PbI₃ thin film exhibit enhanced J_{SC} .

Moreover, by integration of the transient photocurrent densities over the transient times, the total charge densities of PSCs verse the transient times are calculated. Figure 6d shows the integrated charge density of PSCs by either CH₃NH₃PbI₃ or PEO-CH₃NH₃PbI₃ thin films. The total charge densities collected at a long-time scale are almost the same for both PSCs, but the rising time for PSCs by PEO-CH₃NH₃PbI₃ thin film reaches 90% of the value of the total charge density at 185 ns, whereas 348 ns is for PSCs by CH₃NH₃PbI₃ thin film. The faster rising time indicates the efficient charge carrier collection in PSCs by PEO-CH₃NH₃PbI₃ thin film. Therefore, PSCs by PEO-CH₃NH₃PbI₃ thin film have a higher *J*_{SC}.

Figure 7a presents the J-V characteristics of PSCs conducted in the dark. The lower dark current densities in the reverse bias region are observed from PSCs by PEO– $CH_3NH_3PbI_3$ thin film, as compared with those by $CH_3NH_3PbI_3$ thin film. The reduced dark current densities confirm an enlarged V_{OC} from PSCs by PEO– $CH_3NH_3PbI_3$ thin films. Figure 7b displays the capacitance versus voltage characteristics of PSCs. Based on the Mott–Schottky theory, the build-in potential (V_{bi}) of PSCs are extracted from $C^{-2} = \frac{2(V_{bi}-V)}{q\varepsilon\varepsilon_0A^2n_{trap}}$ (where ε is the dielectric constant, ε_0 is the vacuum permittivity, and A is the active area). From the

vacuum permittivity, and A is the active area). From the intercept of C^{2-} –V plot, a $V_{\rm bi}$ of 1.09 V is observed from PSCs by CH₃NH₃PbI₃ thin film, whereas a $V_{\rm bi}$ of 1.18 V is observed from PSCs by PEO–CH₃NH₃PbI₃ thin film. As a result, PSCs

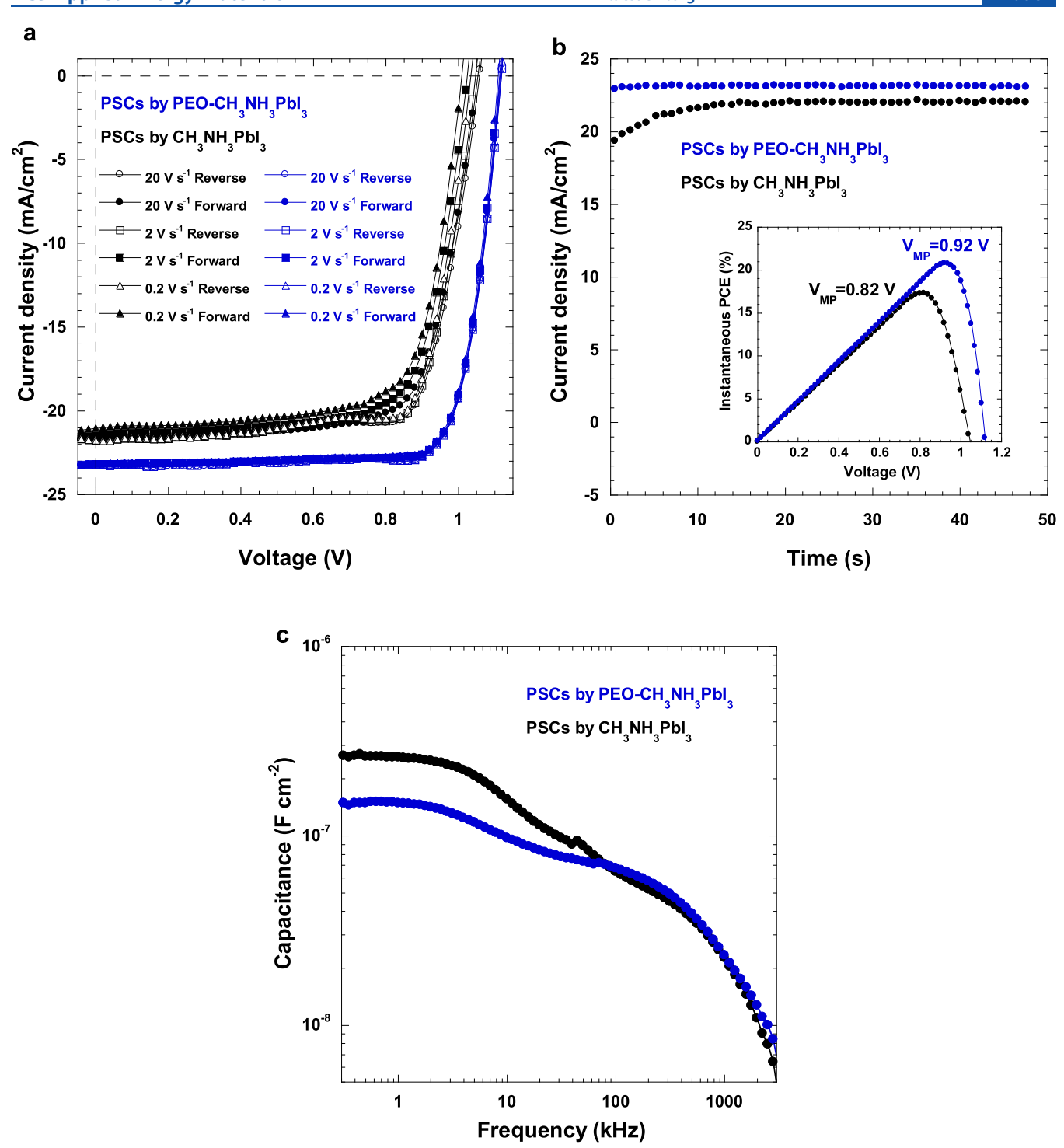


Figure 8. (a) The *J–V* characteristics of PSCs by either CH₃NH₃PbI₃ or PEO–CH₃NH₃PbI₃ thin films under different scan directions and scan rates, (b) the steady-state photocurrents of PSCs by either CH₃NH₃PbI₃ or PEO–CH₃NH₃PbI₃ thin films at the maximum power point voltages, and (c) the *C–F* characteristics of PSCs by either CH₃NH₃PbI₃ or PEO–CH₃NH₃PbI₃ thin films.

by PEO-CH₃NH₃PbI₃ thin film possess a larger $V_{\rm OC}$ than that by PSCs by CH₃NH₃PbI₃ thin film.

Figure 8a displays the J-V characteristics of PSCs under the forward and reverse scan directions at different scan rates. The hysteresis index (HI) is used to describe the photocurrent hysteresis.³³ Table S1 summarizes the device performance parameters and the HI. At the scan rates of 0.2, 2, and 20 V s⁻¹, HI values of 0.106, 0.079, and 0.049 are found from PSCs by $CH_3NH_3PbI_3$ thin film, whereas HI values of 0.009, 0.006, and

0.006 are found from PSCs by PEO– $CH_3NH_3PbI_3$ thin film. These results demonstrate that PSCs by PEO– $CH_3NH_3PbI_3$ thin film possess dramatically suppressed photocurrent hysteresis behavior.

Studies indicated that the trapping and detrapping processes induced by the defects or trap states in the perovskite layer are one of major origins responsible for the photocurrent hysteresis.^{33,34} At a slow scan rate, PSCs are able to undergo the trapping and detrapping processes, and the photocurrents

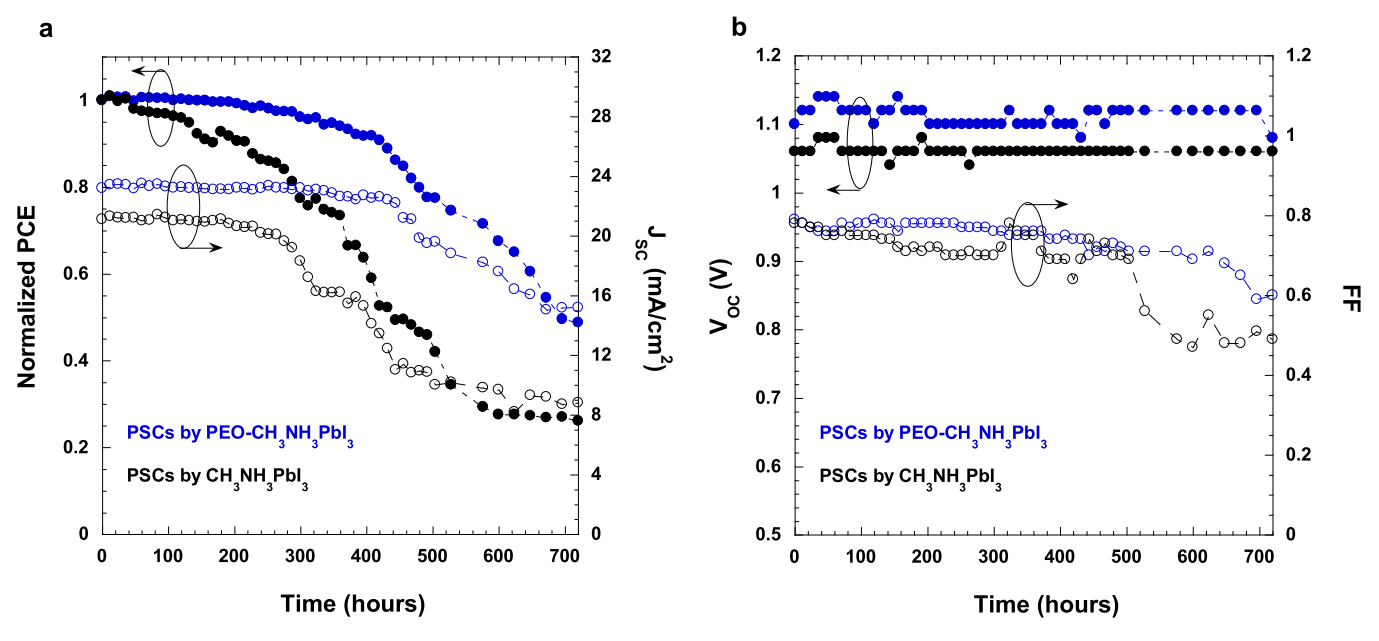


Figure 9. Self-stabilities of PSCs by $CH_3NH_3PbI_3$ and $PEO-CH_3NH_3PbI_3$ thin film in terms of (a) PCE and J_{SC} and (b) V_{OC} and FF.

observed from PSCs under the forward and reverse scan directions would be dramatically different compared to those at a fast scan rate. The noticeable effect of the scan rate on the photocurrent hysteresis behavior indicates that large defects and the trap densities induce serious effects on the trapping and detrapping processes that occurred in PSCs by CH3NH3PbI3 thin film. In comparison, the less effect of scan rate on the photocurrent hysteresis indicates that the defects and the trap densities are minimized, which results in significantly suppressed HI for PSCs by PEO-CH₃NH₃PbI₃ thin film. Figure 8b presents the steady-state photocurrent at the maximum power voltage versus time, where the maximum power voltage is obtained from PCE versus voltage characteristics as shown in the inset of Figure 8b. A slow photocurrent response before reaching the steady-state observed from PSCs by CH3NH3PbI3 thin film indicates an obvious photocurrent hysteresis behavior. Such pronounced photocurrent hysteresis is originated from the trapping and detrapping process on the defects and the trap states within CH₂NH₃PbI₃ thin film.³⁴ As a comparison, there was a negligible photocurrent hysteresis observed from PSCs by PEO-CH3NH3PbI3 thin film, which indicates that the defects and trap states in PEO-CH3NH3PbI3 thin film are dramatically suppressed. In addition, based on Figure 7b, a trap density of 1.65×10^{16} cm⁻³ is estimated from PSCs by CH₃NH₃PbI₃ thin film, whereas a trap density of 7.74×10^{15} cm⁻³ is estimated from PSCs by PEO-CH₃NH₃PbI₃ thin film. A significantly reduced trap density illustrates that the photocurrent hysteresis in PSCs by PEO-CH₃NH₃PbI₃ thin film is dramatically suppressed.

To further investigate the mechanism of suppressed defects and the trap densities in PEO–CH₃NH₃PbI₃ thin film, capacitance versus frequency characteristics analysis of PSCs is performed for dark conditions, and the results are presented in Figure 8c. Both PSCs exhibit a capacitance of $\sim 10^{-7}$ F cm⁻² in the low-frequency region, which indicates the correlation to the interfacial reactive sites.³⁵ PSCs by PEO–CH₃NH₃PbI₃ thin film possess a capacitance of 1.11×10^{-7} F cm⁻², which is lower than that $(2.71 \times 10^{-7}$ F cm⁻²) in PSCs by CH₃NH₃PbI₃ thin film, indicating that PEO–CH₃NH₃PbI₃

thin film possesses less reactive sites. Such diminished reactive sites are attributed to the interactions between PEO and counterions in perovskite, indicating that the counterions are less movable within PSCs by PEO-CH₃NH₃PbI₃ thin film. Therefore, PSCs by PEO-CH₃NH₃PbI₃ thin film possess reduced defects and/or trap densities, resulting in suppressed photocurrent hysteresis.

The shelf-stabilities of both PSCs are also studied. As presented in Figure 9a, for PSCs by PEO-CH₃NH₃PbI₃ thin film, it takes 696 h to degrade PCEs to half of their value, whereas, for PSCs by CH₃NH₃PbI₃ thin film, it takes 444 h to degrade PCEs to their half value. Similarly, it takes 696 h to drop J_{SC} to its half value for PSCs by PEO-CH₃NH₃PbI₃ thin film, whereas the degradation of J_{SC} to its half value takes 396 h for PSCs by CH3NH3PbI3 thin film. Both time dependence results of V_{OC} and FF for PSCs by either CH₃NH₃PbI₃ thin film or PEO-CH₃NH₃PbI₃ thin film are shown in Figure 9b. Both PSCs possess unchanged $V_{\rm OC}$ values for over 700 h, indicating high-quality CH₃NH₃PbI₃ and PEO-CH₃NH₃PbI₃ thin films prepared by the one-step self-assembled method as compared with that by the two-step method. 13 However, degraded FF values are observed from both PSCs. In particular, PSCs by CH3NH3PbI3 thin film exhibit more serious degradation of FF values. Such degradation is probably due to poor film morphology. But nevertheless, enhanced shelf-stability observed from PSCs by PEO-CH₃NH₃PbI₃ thin film demonstrates that PEO is responsible for producing highquality PEO-CH3NH3PbI3 thin film and suppressing the defects and the trap states within PSCs.

4. CONCLUSION

I

In summary, we reported efficient PSCs with dramatically suppressed photocurrent hysteresis and significantly boosted stability, through one-step self-assembling processed methylammonium lead iodide (CH₃NH₃PbI₃) cocrystallized with poly(ethylene oxide) (PEO). It was found that one-step self-assembled PEO-CH₃NH₃PbI₃ thin film exhibited high quality with significantly enlarged crystal grains, as compared with one-step self-assembled CH₃NH₃PbI₃ thin film. Systematical

investigations revealed that the introduction of PEO in $\mathrm{CH_3NH_3PbI_3}$ can improve charge carrier transport, reduce charge carrier recombination, and promote charge carrier charge extraction time. As a result, perovskite solar cells (PSCs) by one-step self-assembled PEO– $\mathrm{CH_3NH_3PbI_3}$ thin film exhibited a J_{SC} of 23.01 mA cm⁻², a V_{OC} of 1.12 V, an FF of 0.81, and a corresponding PCE of 20.78%, which is about a 20% enhancement compared to that by one-step self-assembled $\mathrm{CH_3NH_3PbI_3}$ thin film. Moreover, PSCs by one-step self-assembling processed PEO– $\mathrm{CH_3NH_3PbI_3}$ thin film exhibited significantly suppressed photocurrent hysteresis and boosted stability. Our studies demonstrated a simple way to approach high-performance PSCs.

ASSOCIATED CONTENT

Supporting Information

The Supporting Information is available free of charge at https://pubs.acs.org/doi/10.1021/acsaem.0c00823.

(S1) Device performance of PSCs; (S2) total internal reflection fluorescence microscope images of CH₃NH₃PbI₃ and PEO-CH₃NH₃PbI₃ crystal grains; and (S3) impedance spectra of PSCs by either CH₃NH₃PbI₃ or PEO-CH₃NH₃PbI₃ thin films (PDF)

AUTHOR INFORMATION

Corresponding Author

Xiong Gong — College of Polymer Science and Polymer Engineering. The University of Akron, Akron, Ohio 44325, United States; orcid.org/0000-0001-6525-3824; Email: xgong@uakron.edu; Fax: (330) 9723406

Authors

Luyao Zheng — College of Polymer Science and Polymer Engineering, The University of Akron, Akron, Ohio 44325, United States

Kai Wang — College of Polymer Science and Polymer Engineering, The University of Akron, Akron, Ohio 44325, United States

Tao Zhu – College of Polymer Science and Polymer Engineering, The University of Akron, Akron, Ohio 44325, United States

Yongrui Yang — College of Polymer Science and Polymer Engineering, The University of Akron, Akron, Ohio 44325, United States

Rui Chen – College of Polymer Science and Polymer Engineering, The University of Akron, Akron, Ohio 44325, United States

Kai Gu — College of Polymer Science and Polymer Engineering, The University of Akron, Akron, Ohio 44325, United States

Chunming Liu — College of Polymer Science and Polymer Engineering, The University of Akron, Akron, Ohio 44325, United States

Complete contact information is available at: https://pubs.acs.org/10.1021/acsaem.0c00823

Notes

The authors declare no competing financial interest.

ACKNOWLEDGMENTS

The authors thank the National Science Foundation (EECs 1903303) and the Air Force Office of Scientific Research (AFOSR) (through the Organic Materials Chemistry Program, grant no. FA9550-15-1-0292, Program Manager, Dr. Kenneth Caster) for financial support.

REFERENCES

- (1) Grätzel, M. The rise of highly efficient and stable perovskite solar cells. *Acc. Chem. Res.* **2017**, *50*, 487–491.
- (2) Seo, J.; Noh, J. H.; Seok, S. I. Rational strategies for efficient perovskite solar cells. *Acc. Chem. Res.* **2016**, *49*, 562–572.
- (3) NREL. Research Cell Record Efficiency Chart. 2019; https://www.nrel.gov/pv/assets/pdfs/pv-efficiency-chart.20190103.pdf (accessed 2020).
- (4) Herz, L. M. Charge-carrier dynamics in organic-inorganic metal halide perovskites. *Annu. Rev. Phys. Chem.* **2016**, *67*, *65*–89.
- (5) Walsh, A.; Scanlon, D. O.; Chen, S.; Gong, X.; Wei, S. H. Self-regulation mechanism for charged point defects in hybrid halide perovskites. *Angew. Chem., Int. Ed.* **2015**, *54*, 1791–1794.
- (6) Correa-Baena, J.-P.; Saliba, M.; Buonassisi, T.; Grätzel, M.; Abate, A.; Tress, W.; Hagfeldt, A. Promises and challenges of perovskite solar cells. *Science* **2017**, *358*, 739–744.
- (7) Buin, A.; Pietsch, P.; Xu, J.; Voznyy, O.; Ip, A. H.; Comin, R.; Sargent, E. H. Materials processing routes to trap-free halide perovskites. *Nano Lett.* **2014**, *14*, 6281–6286.
- (8) Agiorgousis, M. L.; Sun, Y.-Y.; Zeng, H.; Zhang, S. Strong covalency-induced recombination centers in perovskite solar cell material CH₃NH₃PbI₃. *J. Am. Chem. Soc.* **2014**, *136*, 14570–14575.
- (9) Snaith, H. J.; Abate, A.; Ball, J. M.; Eperon, G. E.; Leijtens, T.; Noel, N. K.; Stranks, S. D.; Wang, J. T.-W.; Wojciechowski, K.; Zhang, W. Anomalous hysteresis in perovskite solar cells. *J. Phys. Chem. Lett.* **2014**, *5*, 1511–1515.
- (10) Wang, K.; Liu, C.; Yi, C.; Chen, L.; Zhu, J.; Weiss, R.; Gong, X. Efficient perovskite hybrid solar cells via ionomer interfacial engineering. *Adv. Funct. Mater.* **2015**, *25*, 6875–6884.
- (11) Seo, J. Y.; Matsui, T.; Luo, J.; Correa-Baena, J. P.; Giordano, F.; Saliba, M.; Schenk, K.; Ummadisingu, A.; Domanski, K.; Hadadian, M.; et al. Ionic liquid control crystal growth to enhance planar perovskite solar cells efficiency. *Adv. Energy Mater.* **2016**, *6*, 1600767.
- (12) Bai, S.; Da, P.; Li, C.; Wang, Z.; Yuan, Z.; Fu, F.; Kawecki, M.; Liu, X.; Sakai, N.; Wang, J. T.-W.; et al. Planar perovskite solar cells with long-term stability using ionic liquid additives. *Nature* **2019**, *571*, 245–250.
- (13) Wang, K.; Zheng, L.; Zhu, T.; Liu, L.; Becker, M. L.; Gong, X. High performance perovskites solar cells by hybrid perovskites cocrystallized with poly (ethylene oxide). *Nano Energy* **2020**, *67*, 104229.
- (14) Bi, D.; Yi, C.; Luo, J.; Décoppet, J.-D.; Zhang, F.; Zakeeruddin, S. M.; Li, X.; Hagfeldt, A.; Grätzel, M. Polymer-templated nucleation and crystal growth of perovskite films for solar cells with efficiency greater than 21%. *Nat. Energy* **2016**, *1*, 16142.
- (15) Wu, C.; Li, H.; Yan, Y.; Chi, B.; Felice, K. M.; Moore, R. B.; Magill, B. A.; Mudiyanselage, R. R. H. H.; Khodaparast, G. A.; Sanghadasa, M.; Priya, S. Highly-stable organo-lead halide perovskites synthesized through green self-assembly process. *Solar RRL* **2018**, *2*, 1800052.
- (16) Wang, K.; Wu, C.; Hou, Y.; Yang, D.; Li, W.; Deng, G.; Jiang, Y.; Priya, S. A nonionic and low-entropic MA (MMA) nPbI₃-Ink for fast crystallization of perovskite thin films. *Joule* **2020**, *4*, 615.
- (17) Saidaminov, M. I.; Abdelhady, A. L.; Murali, B.; Alarousu, E.; Burlakov, V. M.; Peng, W.; Dursun, I.; Wang, L.; He, Y.; Maculan, G.; et al. High-quality bulk hybrid perovskite single crystals within minutes by inverse temperature crystallization. *Nat. Commun.* **2015**, *6*, 7586.
- (18) Seifter, J.; Sun, Y.; Heeger, A. J. Transient photocurrent response of small-molecule bulk heterojunction solar cells. *Adv. Mater.* **2014**, *26*, 2486–2493.
- (19) Sim, L.; Gan, S.; Chan, C.; Yahya, R. ATR-FTIR studies on ion interaction of lithium perchlorate in polyacrylate/poly (ethylene oxide) blends. *Spectrochim. Acta, Part A* **2010**, *76*, 287–292.
- (20) Acik, M.; Alam, T. M.; Guo, F.; Ren, Y.; Lee, B.; Rosenberg, R. A.; Mitchell, J. F.; Park, I. K.; Lee, G.; Darling, S. B. Substitutional growth of methylammonium lead iodide perovskites in alcohols. *Adv. Energy Mater.* **2018**, *8* (5), 1701726.

- (21) Glaser, T.; Müller, C.; Sendner, M.; Krekeler, C.; Semonin, O. E.; Hull, T. D.; Yaffe, O.; Owen, J. S.; Kowalsky, W.; Pucci, A.; et al. Infrared spectroscopic study of vibrational modes in methylammonium lead halide perovskites. *J. Phys. Chem. Lett.* **2015**, *6* (15), 2913–2918.
- (22) Xu, W.; Hu, Q.; Bai, S.; Bao, C.; Miao, Y.; Yuan, Z.; Borzda, T.; Barker, A. J.; Tyukalova, E.; Hu, Z.; et al. Rational molecular passivation for high-performance perovskite light-emitting diodes. *Nat. Photonics* **2019**, *13* (6), 418–424.
- (23) Yao, X.; Zheng, L.; Zhang, X.; Xu, W.; Hu, W.; Gong, X. Efficient perovskite solar cells through suppressed nonradiative charge carrier recombination by a processing additive. ACS Appl. Mater. Interfaces 2019, 11, 40163–40171.
- (24) Liu, C.; Wang, K.; Yi, C.; Shi, X.; Smith, A. W.; Gong, X.; Heeger, A. J. Efficient perovskite hybrid photovoltaics via alcohol-vapor annealing treatment. *Adv. Funct. Mater.* **2016**, *26*, 101–110.
- (25) Li, N.; Lassiter, B. E.; Lunt, R. R.; Wei, G.; Forrest, S. R. Open circuit voltage enhancement due to reduced dark current in small molecule photovoltaic cells. *Appl. Phys. Lett.* **2009**, *94*, 023307.
- (26) Leong, W. L.; Cowan, S. R.; Heeger, A. J. Differential resistance analysis of charge carrier losses in organic bulk heterojunction solar cells: observing the transition from bimolecular to trap-assisted recombination and quantifying the order of recombination. *Adv. Energy Mater.* **2011**, *1*, 517–522.
- (27) Street, R.; Schoendorf, M.; Roy, A.; Lee, J. Interface state recombination in organic solar cells. *Phys. Rev. B: Condens. Matter Mater. Phys.* **2010**, *81*, 205307.
- (28) Shuttle, C. G.; O'Regan, B.; Ballantyne, A. M.; Nelson, J.; Bradley, D. D.; Durrant, J. R. Bimolecular recombination losses in polythiophene: fullerene solar cells. *Phys. Rev. B: Condens. Matter Mater. Phys.* **2008**, 78, 113201.
- (29) Groves, C.; Greenham, N. Bimolecular recombination in polymer electronic devices. *Phys. Rev. B: Condens. Matter Mater. Phys.* **2008**, 78, 155205.
- (30) Li, Z.; Wang, W.; Greenham, N. C.; McNeill, C. R. Influence of nanoparticle shape on charge transport and recombination in polymer/nanocrystal solar cells. *Phys. Chem. Chem. Phys.* **2014**, *16*, 25684–25693.
- (31) Cowan, S. R.; Leong, W. L.; Banerji, N.; Dennler, G.; Heeger, A. J. Identifying a threshold impurity level for organic solar cells: Enhanced first-order recombination via well-defined PC84BM traps in organic bulk heterojunction solar cells. *Adv. Funct. Mater.* **2011**, *21*, 3083–3092.
- (32) Schroder, D. K. Semiconductor Material and Device Characterization; John Wiley & Sons: 2015.
- (33) Sanchez, R. S.; Gonzalez-Pedro, V.; Lee, J.-W.; Park, N.-G.; Kang, Y. S.; Mora-Sero, I.; Bisquert, J. Slow dynamic processes in lead halide perovskite solar cells. Characteristic times and hysteresis. *J. Phys. Chem. Lett.* **2014**, *5*, 2357–2363.
- (34) Chen, B.; Yang, M.; Priya, S.; Zhu, K. Origin of J-V hysteresis in perovskite solar cells. *J. Phys. Chem. Lett.* **2016**, *7*, 905–917.
- (35) Kim, H.-S.; Jang, I.-H.; Ahn, N.; Choi, M.; Guerrero, A.; Bisquert, J.; Park, N.-G. Control of I–V hysteresis in CH₃NH₃PbI₃ perovskite solar cell. *J. Phys. Chem. Lett.* **2015**, *6*, 4633–4639.